Shape tailored Cu_2ZnSnS_4 nanosheet aggregates for high efficiency solar desalination

Jin Zhang[a,*], Yawei Yang[b], Jianqiu Zhao[b], Zhonghua Dai[a], Weiguo Liu[a], Chaobo Chen[c], Song Gao[c], D.A. Golosov[d], S.M. Zavadski[d], S.N. Melnikov[d]

[a] *Shaanxi Province Key Laboratory of Thin Films Technology and Optical Test, School of Optoelectronic Engineering, Xi'an Technological University, Xi'an, 710032, PR China*
[b] *Electronic Materials Research Laboratory, Key Laboratory of the Ministry of Education, International Center for Dielectric Research, and Shaanxi Engineering Research Center of Advanced Energy Materials and Devices, School of Electronic & Information Engineering, Xi'an Jiaotong University, Xi'an, 710049, PR China*
[c] *School of Electronic Information Engineering, Xi'an Technological University, Xi'an, 710032, PR China*
[d] *Belarusian State University of Informatics and Radioelectronics, 6 P. Brovka Str., 220013, Minsk, Belarus*

ARTICLE INFO

ABSTRACT

In this paper, the shape tailored high-purity kesterite phase Cu_2ZnSnS_4 (CZTS) nanosheet aggregates (NSAs) were prepared in a low cost one-pot solvothermal method, and further fabricated into a salt-blocking membrane for solar desalination. The designed CZTS NSAs membrane-based solar steam generation device featured high solar absorptivity, low thermal energy loss and long-term stability, achieving a remarkable water evaporation rate of 1.54 kg/m²h and solar steam conversion efficiency of 78.85%. It is noteworthy that the quality of artificial seawater desalinated by evaporation was better than that of distilled water, and organic dyes, in particular, could be degraded by nearly 100%. It indicates that the CZTS NSAs membrane is likely to be one of the greatest potential substitutes for seawater desalination as well as repurification of urban reclaimed water and chemical wastewater.

1. Introduction

As a renewable energy source, solar energy has received increasing attention. It is considerably preferred for its unique advantages such as complete cleanness, unlimited reserves, and many advantages like minimum operating cost, no consumption of conventional energy, no secondary pollution; it is especially gradually valued and widely used as a substitute for conventional energy in water treatment. At present, it is one of the mainstream technologies for the development and application of new energy and new water resources [1–5].

Currently, the efficiency of wastewater or seawater treatment by conventional solar steam evaporation is relatively low, about 3–4 kg/m²/d. In recent years, a new method of solar energy evaporating and purifying wastewater or seawater assisted by a black membrane has sparked extensive concern of academic circles. The method is that the black carbon materials (graphene, carbon nanotubes and graphene oxide) or nanometal particles adopted were suspended in the liquid level and fully immersed in the wastewater or seawater; under the sunlight, the black materials absorbed most of the sunlight energy and restrained the heat on the liquid surface, which greatly improved the

evaporation efficiency of water [6–12].

After a review of the research achievements in water treatment by the solar energy in recent years, it is not difficult to find that such research was focused on auxiliary materials for photothermal conversion. The auxiliary materials used in literature mainly included SiO_2/Au nanoshells [6], Au nanoparticles [10], PPY [7], graphene [8], graphene oxide [11], carbon nanotubes [9], alumina sheets decorated with aluminum nanoparticles [12] and so on. However, it is not practical to accelerate the evaporation rate by using the plasmon effect caused by a precious metal like SiO_2/Au nanoshells or Au nanoparticles. On the one hand, the preparation of precious metals is expensive, which is not helpful for large-scale use. On the other hand, it's not good for recycling, either. PPY is an organic material that will age and decompose under the sunlight for a long time, thus it is not an ideal auxiliary material for photothermal conversion. Porous alumina sheet is a fragile material, and the cost of preparation is high, which is not conducive to mass production.

Due to high photothermal conversion efficiency, good stability and easy recycling, graphene, graphene oxide and carbon nanotubes seem to be suitable used for desalination [8,9,11]. It is worth mentioning that

the all-in-one 3D cross-linked honeycomb graphene-based device reported by Y. Yang et al, its specific water production rate has achieved 2.6 kg/ m^2 h g (1.3 kg/m^{2}h) [13]. But the cost of graphene ($ 4,500/kg) and carbon nanotubes ($ 1,000/kg) is relatively high at this stage. Recently, the black photoelectric semiconductor materials, which are stable in chemical property, non-toxic, easy for synthesis and less expensive, have attracted more attentions in photothermal conversion [14–19]. Especially in seawater desalination, it has shown remarkable properties, such as: anti-bacteria, photocatalytic effect and high water production rate, which proved that the black photoelectric semiconductor materials are potential alternative auxiliary materials for desalination [20–26]. However, there are still many problems remain to be solved. For example, C. Mu, et al. prepared CZTS nanosheet films on the conductive glass in the electrophoresis method, and the assisted solar evaporation rate reached 1.46 kg/m^2/h [25]. But the CZTS nanosheet film was required to be fully immersed in water due to the experimental device, which could not effectively reduce heat loss. In our research group, Yang et al. adopted Cu$_2$SnSe$_3$, a hydrophobic/hydrophilic bilayer structure, to prepare an auxiliary evaporation film with solar evaporation rate 1.657 kg/m^2/h [26]. However, due to the solubility of Se source in preparation process, it is not suitable for mass production.

In this paper, the kesterite phase CZTS NSAs were prepared in a low cost one-pot solvothermal method, and their shapes could be controlled by concentrations of precursor solutions. Furthermore, the salt-blocking CZTS NSAs-based filter membranes were fabricated and applied in a designed solar steam generation device; the evaporation and desalination performance of the CZTS NSAs membrane-based device were also investigated.

2. Experiment

2.1. Synthesis of CZTS NSAs

The CZTS NSAs were prepared via solvothermal method. Firstly, 0.45 g of Polyvinylpyrrolidone (PVP) was dissolved in ethylene glycol (EG), and then the 12.5 mM of CuCl$_2$·2H$_2$O, 6.25 mM of ZnCl$_2$ and 6.25 mM of SnCl$_4$·5H$_2$O were added in and dissolved by magnetic stirring. When the 31.25 mM of thiourea (Tu) was added and dissolved, the solution become clear light-yellow, which can be served as the precursor solution of CZTS NSAs. Next, the precursor solution was sealed into a hydrothermal reactor and heated at setting temperatures (140, 160, 180 and 200 °C) for 24 h. After being cooled to room temperature, the obtained black colloidal solution was washed by deionized water and ethanol several times. Finally, the CZTS NSAs were obtained after the products were vacuum-dried at 60 °C for several minutes. The concentration of precursor solution mentioned above was marked as C$_1$, and the double and quadruple concentrations as C$_2$ and C$_3$ respectively.

2.2. Fabrication of CZTS NSAs membrane and the solar desalination device

To prevent blocking of the waterways caused by salt accumulation during evaporation of seawater, the low surface energy treatment of CZTS NSAs was first carried out as previously reported in Ref. [27,28]. The solution of 1% volume ratio, which contains of isopropyl alcohol (97.5 vol.%), Perfluoro-octylethyl trimethoxy silane (2.0 vol.%) and glacial acetic acid (0.5 vol.%), was added to the aqueous suspension of CZTS NSAs. Then, the aqueous suspension of CZTS NSAs, containing the determined mass (2, 4, 6, 8 and 10 mg), was pumped onto a 0.22 μm filter membrane to form a piece of CZTS NSAs membrane. Finally, the membrane was dried under vacuum at 110 °C for 2 h. The simple solar desalination experimental device and its components are showed in Fig. 7(a) and (b). The CZTS NSAs membrane is served as the auxiliary photothermal conversion and photocatalytic component, the water conducts via a piece of nonwoven fabric through capillary effect and a
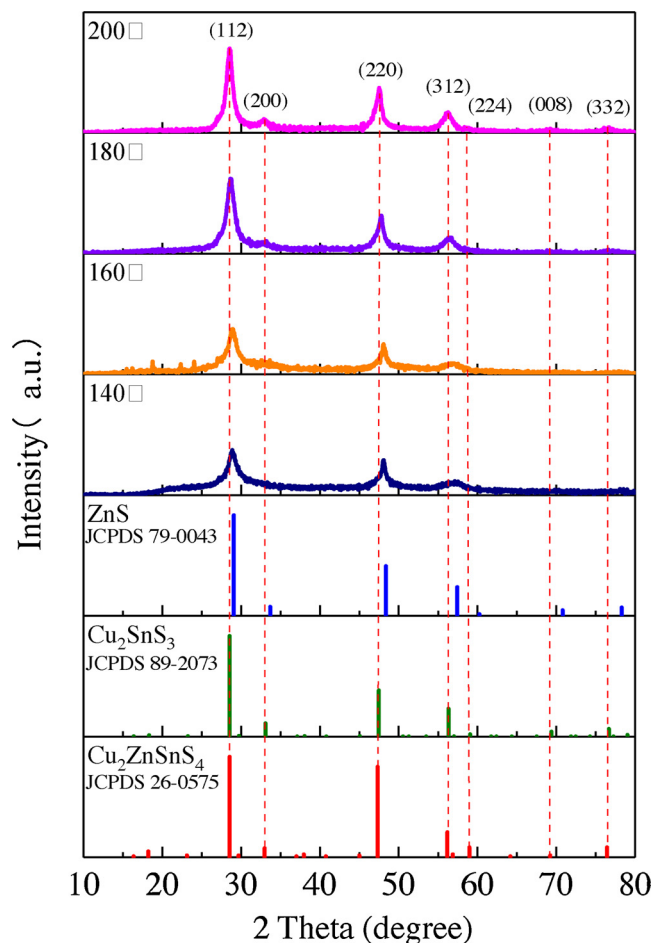
Fig. 1. XRD patterns of as-prepared CZTS samples grown at different solvothermal temperatures.

polystyrene foam was employed to block the heat transfer between evaporation layer and water source.

2.3. Characterization of CZTS NSAs

The structural properties of the CZTS NSAs samples were detected by X-ray diffraction (XRD) spectrometer (D8 ADVANCE, Bruker AXS, German). The morphological property was observed with a field-emission scanning electron microscopy (GeminiSEM 500, Zeiss, German). Raman testing and analysis were used a laser Raman spectroscope (LabRAM HR Evolution, HORIBA, Japan) with a 532 nm line for the excitation. The UV–vis-NIR spectra were tested on an UV–vis-NIR spectrometer (LAMBDA950, PerkinElmer, American). The specific surface area of the CZTS NSAs samples were tested by an automatic gas adsorption analyzer (Autosorb-iQ, Quantachrome, American).

2.4. Solar evaporation test of CZTS NSAs membrane-based device under AM 1.5 irradiation

The solar evaporation test was carried out on the CZTS NSAs membrane, which was cut into a piece of 2 × 2 cm^2. The CZTS NSAs membrane-based device was irradiated by an AM 1.5 standard light source (Newport, American) at room temperature of 20–25 °C and air humidity at 30–50%. The artificial seawater, which was composed of K$_2$SO$_4$ (1 g/L), NaCl (27.5 g/L), CaCl$_2$ (1.2 g/L) and MgCl$_2$ (5.3 g/L), was prepared according to the scheme as reported in Ref. [25]. In consideration of the pollution source of urban recycled water, the CdCl$_2$ (1.63 g/L), CrCl$_3$ (3.045 g/L), CuCl$_2$ (2.11 g/L) and PbNO$_3$ (1.3 g/L)
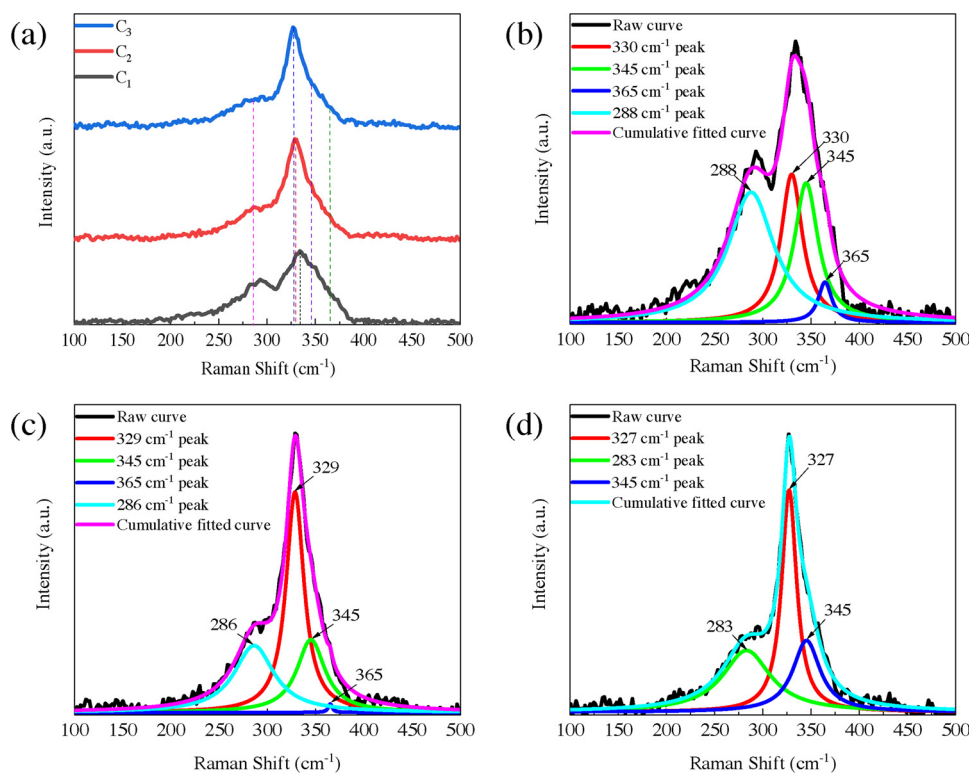
Fig. 2. Raman scattering analysis of CZTS NSAs prepared with different concentrations of precursor solutions. (a) Raman spectra of CZTS NSAs prepared with precursor solutions of C_1, C_2 and C_3 concentrations. (b)–(d) Raman peak fitting of C_1, C_2 and C_3 samples, respectively.
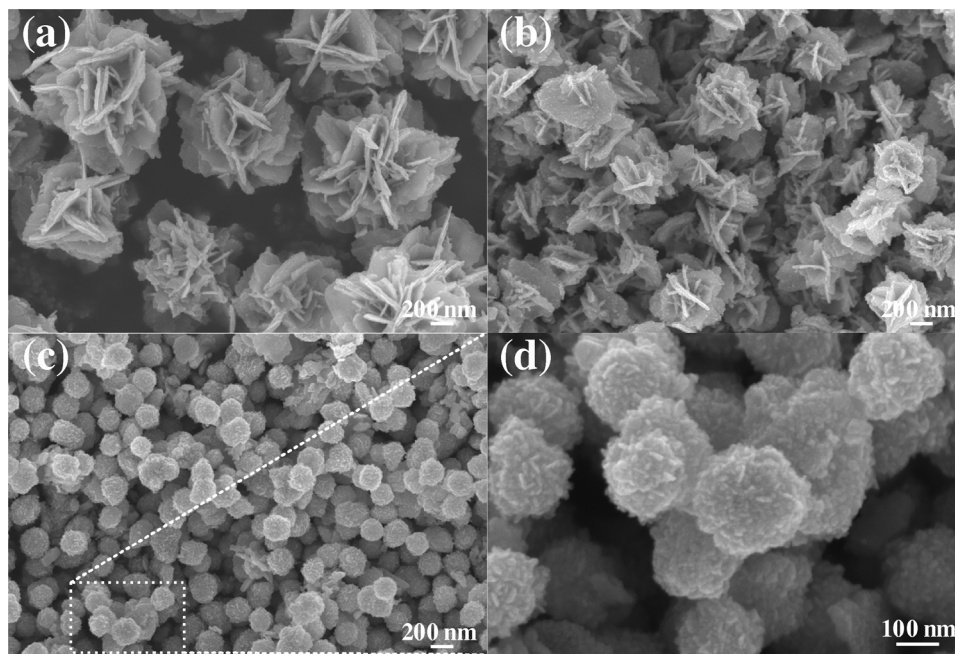
Fig. 3. SEM patterns of as-prepared CZTS samples prepared with different concentration precursor solutions ((a) C_1, (b) C_2 and (c) C_3). (d) Partial enlarged the SEM pattern in Fig. 1(c).

were also added to the artificial seawater. What's more, simulated organic wastewater samples methyl blue (MB), Rhodamine B (RhB) and methyl orange (MO) with concentration of 20 mg/L, 10 mg/L and 20 mg/L were also prepared and tested, respectively. The temperature of the membrane was tested by the FlirOne IR camera. The real-time water weight was monitored by an electronic analytical scale (BSA224S, Sartorius, 0.1 mg in accuracy) during the evaporation process. The solar steam conversion efficiency was estimated via the

calculation method as previously reported in Refs. [26,28]. The inductively coupled plasma spectroscopy (ICP-OES, Optima 8000) was used to measure the ion concentrations of seawater before and after evaporation. The UV/Vis/NIR spectrometer was also used to investigate the degradation of organic dyes.
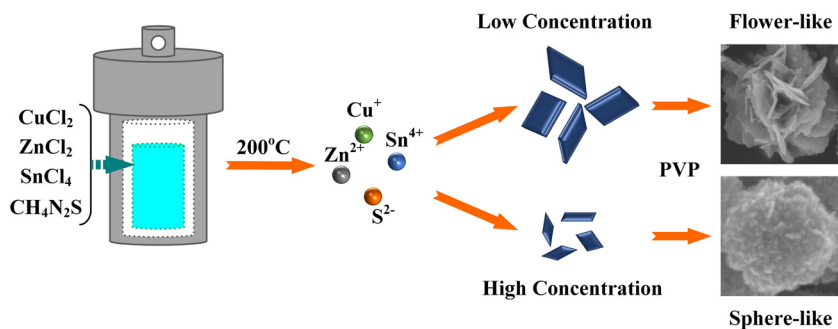
Fig. 4. Schematic diagram of CZTS NSAs formation in different shapes.
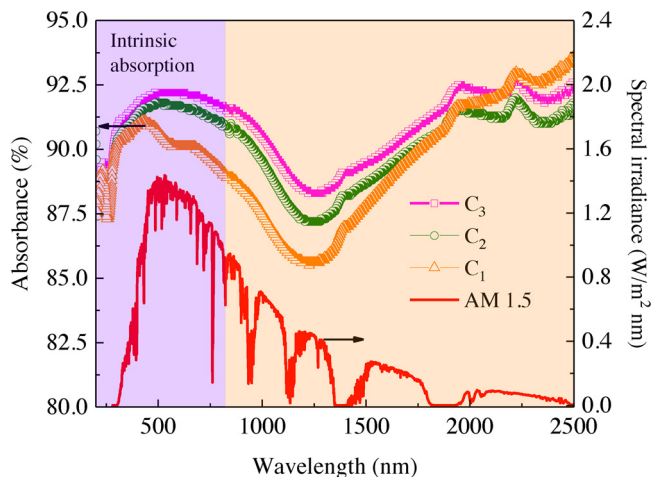
Fig. 5. UV–vis-NIR absorption spectra of C_1, C_2 and C_3 CZTS NSAs samples compared with AM 1.5 solar spectrum.
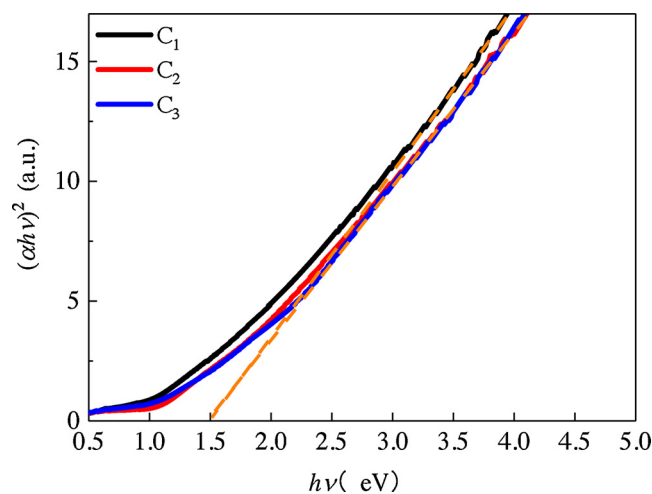
Fig. 6. $(\alpha h\nu)^2$ versus $h\nu$ curve of C_1, C_2 and C_3 CZTS NSAs samples.

3. Results and discussion

The XRD patterns of as-prepared CZTS samples with different grown temperatures are showed in Fig. 1. As we know, the diffraction peaks of the kesterite phase CZTS is almost the same as that of ZnS and Cu_2SnS_3. In order to observe the tiny changes of the peaks, the standard peaks of ZnS and Cu_2SnS_3 are also listed in Fig. 1. From the patterns, it can be seen that the peaks of the as-prepared CZTS grown at 140 °C are more likely to match the standard peaks of ZnS than other samples. The diffraction intensity of the peaks gradually increased with the rising growth temperature and the peaks gradually shifted to the low degree.

Finally, the diffraction peaks of the sample grown at 200 °C desirably matched (112), (200), (220), (312), (224), (008) and (332) planes of kesterite phase CZTS, and no other obvious impurity peaks could be observed, which indicates that 200 °C is the appropriate growth temperature.

The standard XRD peak position of the kesterite phase CZTS is almost identical with that of Cu_2SnS_3 as shown in Fig. 1. Therefore, the Raman spectra of the CZTS NSAs samples were further investigated and analyzed to distinguish the impurities of the samples. Fig. 2 shows the Raman scattering analysis of CZTS NSAs prepared with different concentrations of precursor solutions. According to Fig. 2(a), the main peaks at around $330\,cm^{-1}$ and two shoulders near 285 and $345\,cm^{-1}$ could be clearly observed. In order to accurately calibrate the peak position of these Raman spectra, these peaks were further fitted. The Raman spectrum of C_1 sample could be perfectly fitted to the four peaks which located at 288, 330, 345 and $365\,cm^{-1}$ as shown in Fig. 2(b). Similarly, the fitted peaks of C_2 sample are at 286, 329, 345 and $365\,cm^{-1}$ while that of C_3 sample are at 283, 327 and $345\,cm^{-1}$ as shown in Fig. 2(c) and (d). The main peaks (330, 329 and $327\,cm^{-1}$) of three Raman spectra can be identified as the characteristic phase of CZTS (Mode-A). As is known to all, the universally acknowledged Mode-A peak of CZTS is $331\text{-}339\,cm^{-1}$ [29–31]. There are two main reasons for the low shift of the peaks. One is the crystalline orientation of the CZTS NSAs. The main peak of CZTS will low shift when the crystalline orientation changes from wurtzite to kesterite phase [32,33]; The other is the phonon confinement within the CZTS nanosheets as reported in Ref. [34,35]. The fitted peaks (288, 286 and $283\,cm^{-1}$) located at low wavenumber of the three Raman spectra also belong to the vibration Mode-A of kesterite CZTS. The shoulder that appeared at a high wavenumber of the three Raman spectra can be fitted to two peaks 345 and $365\,cm^{-1}$ which are attributed to Mode E-TO LO and Mode E/B-TO LO of kesterite CZTS [36–39], respectively. In addition, there are no other obvious peaks caused by by-products such as ZnS ($349\text{–}355\,cm^{-1}$), SnS ($190\text{–}196\,cm^{-1}$), Cu_2SnS_3 ($300\text{–}305$, 256 and $267\,cm^{-1}$), Cu_xS ($470\text{–}475\,cm^{-1}$), SnS_2 ($315\,cm^{-1}$), Cu_3SnS_4 ($318\,cm^{-1}$) and Sn_2S ($307\,cm^{-1}$) [39,40] appearing in the three Raman spectra, which indicates that the high purity kesterite phase CZTS NSAs can be obtained in the low cost one-pot solvothermal method.

The SEM patterns of as-prepared CZTS samples prepared with different concentration precursor solutions at 200 °C for 24 h are shown in Fig. 3. It can be clearly observed that the precursor concentration has significant effect on the morphology and size of the CZTS NSAs. Obviously, the size of the CZTS NSAs shrank from about 1 μm to 500 nm while the concentration of the precursors varied from C_1 to C_2, and the morphology of these aggregates is flower-like, as shown in Fig. 3(a) and (b). Interestingly, the CZTS NSAs become monodisperse sphere-like particles when the concentration of the precursor is further enhanced to C_3, and the particle is further reduced to about 200 nm, as shown in Fig. 3(c). What is noteworthy is that these sphere-like CZTS particles are also aggregated from tiny nanosheets which could be clearly observed in Fig. 3(d). This phenomenon can be explained through a
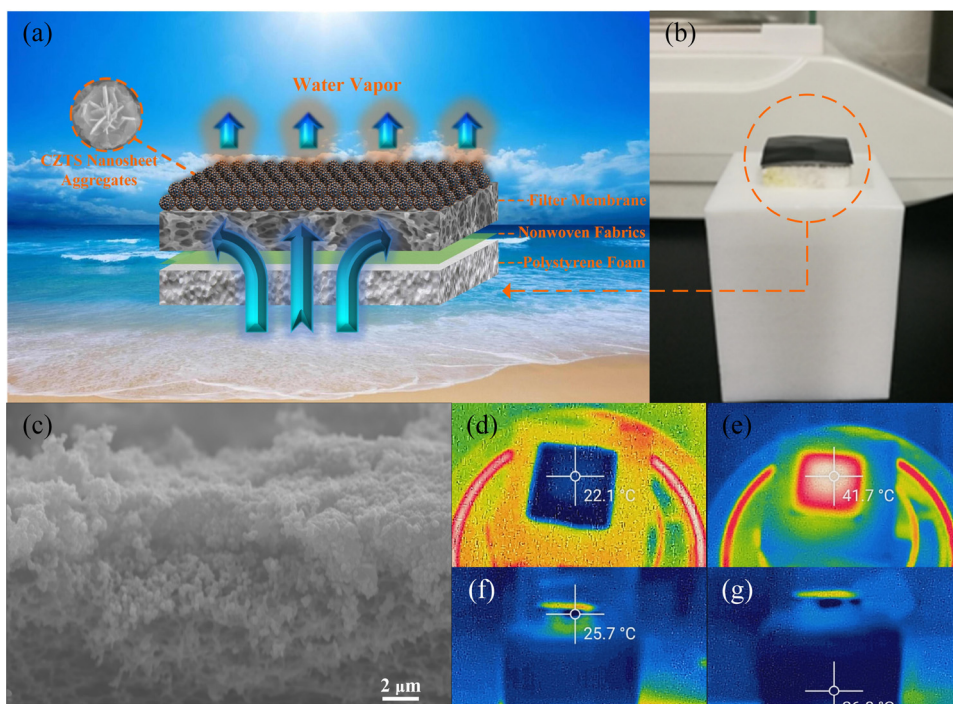
Fig. 7. (a) Schematic illustration of the CZTS NSAs membrane-based solar desalination device. (b) Digital photograph of the solar desalination device. (c) Cross-section SEM pattern of the C_3 CZTS NSAs membrane. (d)–(g) IR images of the solar desalination device while the water evaporation process is over time.
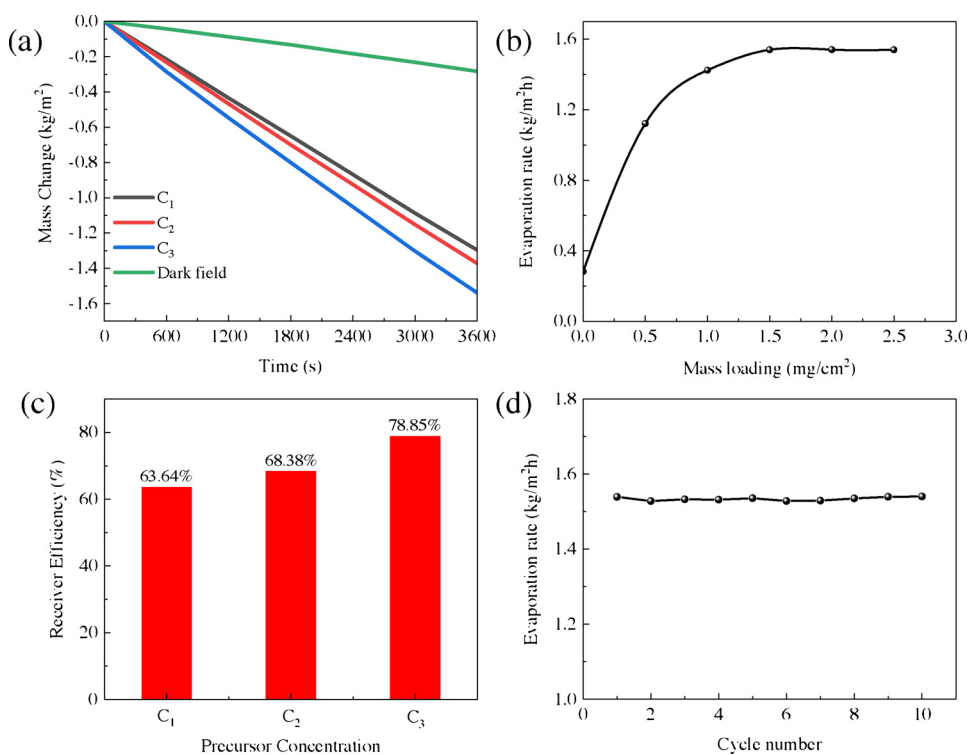
Fig. 8. (a) Real-time seawater weight loss through evaporation by using 10 mg C_1, C_2 and C_3 CZTS NSAs loaded membranes. (b) Evaporation rate of C_3 CZTS NSAs membranes with different loading mass. (c) Solar steam conversion efficiency of C_1, C_2 and C_3 CZTS NSAs (1.5 mg/cm^2) membranes. (d) Evaporation cycle performance of the C_3 CZTS NSAs (1.5 mg/cm^2) membrane.

kinetics mechanism and will be discussed as below.

The above experimental results show that the shape tailored pure kesterite phase CZTS NSAs can be synthesized by the solvothermal method with different concentration precursor solutions. Fig. 4 shows the schematic diagram of CZTS NSAs formation in different shapes. At first, the metal salt and Tu were dissolved in EG to form metal-Tu complexes. With the rising of the temperature, the metal-Tu was thermal dissociated into metal ions, and the Cu^{2+} ions were further

reduced to Cu^+ due to the reduction of EG. Then the metal ions spontaneously formed the CZTS crystal nucleus at the solvothermal temperature, and the CZTS nanosheets were gradually formed via self-assembly of the CZTS crystal nucleus due to the grain rotation induced grain coalescence (GRIGC) mechanism [41]. At the same time, the CZTS nanosheets aggregated to form particles under the polymerization of PVP. In the dynamic balance of crystal growth and nanosheets aggregation, the aggregation probability (collision probability) of the
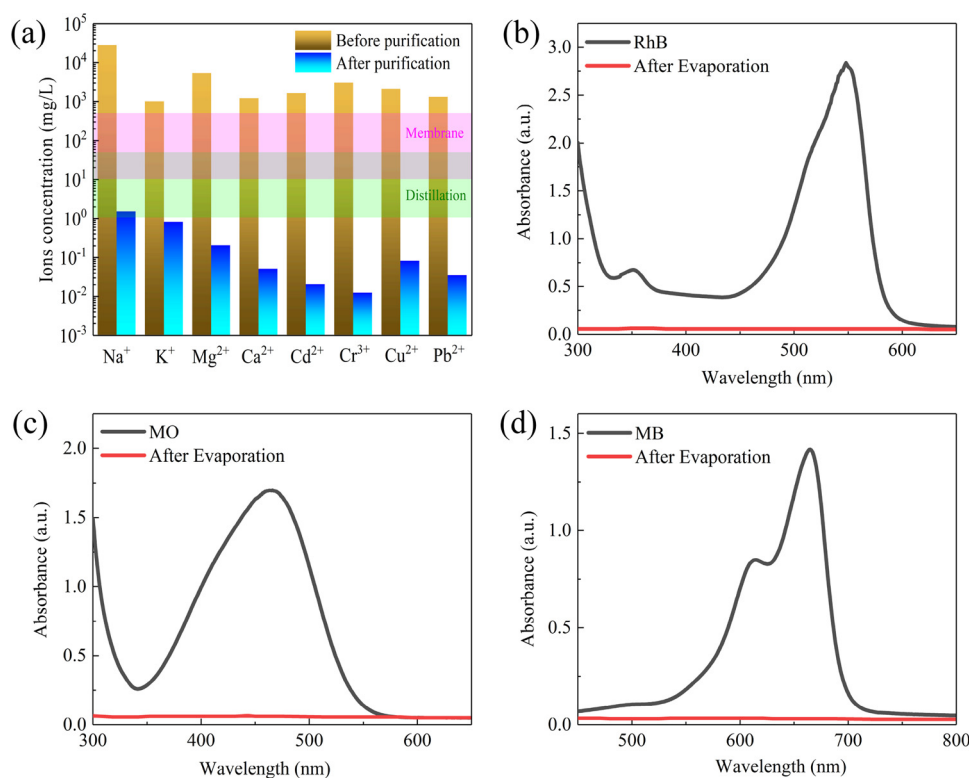
Fig. 9. (a) Ion concentrations of artificial seawater before and after purification. Absorption spectra of RhB (b), MO (c) and MB (d) solutions before and after evaporation.

CZTS nanosheets in high concentration solution was much higher than that in low concentration solution. Therefore, the CZTS nanosheets could grow sufficiently in the low concentration solution and form large size flower-like aggregates under the competitive relationship between crystal growth and nanosheets aggregation. Conversely, the small CZTS nanosheets were aggregated before they were fully grown in the high concentration solution, resulting in small size sphere-like aggregates.

The comparison of the optical absorption spectra of C_1, C_2 and C_3 CZTS NSAs samples with AM 1.5 solar spectrum is demonstrated in Fig. 5. It can be seen that the average absorption efficiency of the samples is around 90% throughout the whole AM 1.5 solar spectrum, which indicates a great application potential in solar energy devices. In addition, the intrinsic absorption of the samples occupies more than half of the total light energy of AM 1.5 spectrum, and the C_3 sample shows the highest absorption efficiency. As a direct bandgap semiconductor, the optical bandgap (E_g) of CZTS samples can be estimated by through classical Tauc's relation [42]:

$$(\alpha h\nu)^2 = A\ (h\nu - E_g) \tag{1}$$

where $h\nu$, α and A are photon energy, adsorption coefficient and a constant respectively, and the Tauc's plot of C_1, C_2 and C_3 samples are shown in Fig. 6. By extrapolating the straight portion of $(\alpha h\nu)^2$ versus $h\nu$ curves to the point $\alpha = 0$, the optical bandgaps of these three samples are estimated to be the same value (1.5 eV), which is coincide with the CZTS bandgap value reported in other literatures [43–45]. It can be claimed that the as-prepared CZTS NSAs not only has high purity, but also is the ideal direct bandgap solar absorbing material.

Fig. 7(a) shows the schematic illustration of the CZTS NSAs membrane-based solar desalination device, where the CZTS NSAs were pumped on the filter membrane as a light absorber and a piece of water conducting nonwoven fabrics was coved on a thermal insulating polystyrene foam. The digital photographs of the solar desalination device are shown in Fig. 7(b). Fig. 7(c) shows the cross-section SEM pattern of the C_3 CZTS NSAs membrane. It can be seen that a part of CZTS NSAs is

embedded in the filter membrane, which means the CZTS layer is not easy to fall off from the filter membrane. The initial temperature of the CZTS NSAs membrane without light irradiation is about 22 °C as shown in Fig. 7(d), and the temperature of the membrane will go up steadily to reach constant within 3–6 min (Fig. 7(e)) after illumination began. From the Fig. 7(f) and (g), it can be seen that the thermal energy is limited in the CZTS NSAs membrane, which indicates the low heat loss in the photothermal conversion process.

The evaporation rate of 10 mg (2.5 mg/cm²) C_1, C_2 and C_3 CZTS NSAs loaded membranes under AM 1.5 are 1.297, 1.373 and 1.539 kg/m²h, respectively, which is more than 4–5 times higher than that of the membranes in the dark field (0.283 kg/m²h) as shown in Fig. 8(a). The C_3 CZTS NSAs membrane shows the best evaporation performance which seems to correlate with the specific surface area of each sample. Therefore, the specific surface area of C_1, C_2 and C_3 samples were also tested. Results show that the specific surface area of C_3 CZTS NSAs up to 149.53 m²/g which is much higher than that of C_1 (22.06 m²/g) and C_2 (35.14 m²/g). Higher specific surface area means more incident light can be absorbed by the C_3 sample and converted into heat, which coincides with the results of optical absorption spectra analysis as shown in Fig. 5. The Fig. 8(b) shows a stable evaporation rate of ˜1.54 kg/m²h is achieved when more than 1.5 mg/cm² of C_3 CZTS NSAs were loaded on the filter membrane. After calculation, the C_3 CZTS NSAs membrane also achieves the highest solar steam conversion efficiency (78.85%) under only one sun as shown in Fig. 8(c). The durability of the C_3 CZTS NSAs membrane is also investigated, and the cycle solar steam generation performance of the C_3 CZTS NSAs membrane is exhibited in Fig. 8(d). It can be clearly observed that the evaporation performance is stable in at least 10 cycles with each cycle sustained for 1 h.

In order to evaluate the water quality, the ion concentrations of artificial seawater before and after evaporation was detected as shown in Fig. 9(a). The ion concentrations of ordinary seawater and four added heavy metal ions are significantly decreased below the values typically obtained through other membrane-based (10–500 ppm) and

distillation-based (1–50 ppm) seawater desalination technologies [26]. The CZTS NSAs membrane could not only accelerate evaporation of seawater, but also degrade organic compounds under the sun light irradiation due to the visible light photocatalysis of CZTS. From Fig. 9(b)–(d), it can be seen that the device achieved nearly 100% rejection rate of RhB, MO and MB, which indicates that such purification mechanism also can be used in treatment of urban reclaimed water and chemical wastewater.

4. Conclusions

In summary, the shape tailored kesterite phase CZTS NSAs have been prepared by a low cost one-pot solvothermal method. Meanwhile, the CZTS NSAs-based filter membrane has also been fabricated and successfully applied in a solar desalination device to be severed as the light absorption and vapor evaporation layer. The CZTS NSAs membrane-based device presents a remarkable solar evaporation rate of ˜1.54 kg/m^{2}h and solar steam conversion efficiency of 78.85% under one sun irradiation due to its unique characteristics such as high-efficiency solar absorption, low thermal energy loss, large specific surface area and long-time durability. Besides, the CZTS NSAs membrane shows the excellent purification effect on metal ions and organic dyes, which indicates that CZTS NSAs is an alternative solar vapor generation material both in seawater desalination and devices for solar steam purification of urban reclaimed water and chemical wastewater.

Acknowledgments

References

[1] N.S. Lewis, Research opportunities to advance solar energy utilization, Science 351 (2016) aad1920.
[2] V.H. Dalvi, S.V. Panse, J.B. Joshi, Solar thermal technologies as a bridge from fossil fuels to renewables, Nat. Clim. Change 5 (2015) 1007–1013.
[3] M.A. Shannon, P.W. Bohn, M. Elimelech, J.G. Georgiadis, B.J. Mariñas, A.M. Mayes, Science and technology for water purification in the coming decades, Nature 452 (2008) 301–310.
[4] Y. Wang, L. Zhang, P. Wang, Self-floating carbon nanotube membrane on macroporous silica substrate for highly efficient solar-driven interfacial water evaporation, ACS Sustain. Chem. Eng. 4 (2016) 1223–1230.
[5] M.S. Zielinski, J.-W. Choi, T. La Grange, M. Modestino, S.M.H. Hashemi, Y. Pu, S. Birkhold, J.A. Hubbell, D. Psaltis, Hollow mesoporous plasmonic nanoshells for enhanced solar vapor generation, Nano Lett. 16 (2016) 2159–2167.
[6] O. Neumann, A.S. Urban, J. Day, S. Lal, P. Nordlander, N.J. Halas, Solar vapor generation enabled by nanoparticles, ACS Nano 7 (2013) 42–49.
[7] L. Zhang, B. Tang, J. Wu, R. Li, P. Wang, Hydrophobic light-to-heat conversion membranes with self-healing ability for interfacial solar heating, Adv. Mater. 27 (2015) 4889–4894.
[8] Y. Ito, Y. Tanabe, J. Han, T. Fujita, K. Tanigaki, M. Chen, Multifunctional porous graphene for high-efficiency steam generation by heat localization, Adv. Mater. 27 (2015) 4302–4307.
[9] C. Chen, Y. Li, J. Song, Z. Yang, Y. Kuang, E. Hitz, C. Jia, A. Gong, F. Jiang, J.Y. Zhu, B. Yang, J. Xie, L. Hu, Highly flexible and efficient solar steam generation device, Adv. Mater. (2017) 1701756.
[10] Z. Wang, Y. Liu, P. Tao, Q. Shen, N. Yi, F. Zhang, Q. Liu, C. Song, D. Zhang, W. Shang, T. Deng, Bio-inspired evaporation through plasmonic film of nanoparticles at the air–water interface, Small 10 (2014) 3234–3239.
[11] X. Lia, W. Xua, M. Tang, L. Zhou, B. Zhu, S. Zhu, J. Zhu, Graphene oxide-based efficient and scalable solar desalination under one sun with a confined 2D water path, PNAS 113 (2016) 13953–13958.
[12] L. Zhou, Y. Tan, J. Wang, W. Xu, Y. Yuan, W. Cai, S. Zhu, J. Zhu, 3D self-assembly of aluminium nanoparticles for plasmon-enhanced solar desalination, Nat. Photonics

[13] Y. Yang, R. Zhao, T. Zhang, K. Zhao, P. Xiao, Y. Ma, P.M. Ajayan, G. Shi, Y. Chen, Graphene-based standalone solar energy converter for water desalination and purification, ACS Nano 12 (2018) 829–835.
[14] W. Guo, C. Guo, N. Zheng, T. Sun, S. Liu, Cs$_x$WO$_3$ nanorods coated with polyelectrolyte multilayers as a multifunctional nanomaterial for bimodal imaging-guided photothermal/photodynamic cancer treatment, Adv. Mater. 29 (2017) 1604157.
[15] W. Ren, Y. Yan, L. Zeng, Z. Shi, A. Gong, P. Schaaf, D. Wang, J. Zhao, B. Zou, H. Yu, G. Chen, E.M.B. Brown, A. Wu, A near infrared light triggered hydrogenated black TiO$_2$ for cancer photothermal therapy, Adv. Healthc. Mater. 4 (2015) 1526–1536.
[16] C.M. Hessel, V.P. Pattani, M. Rasch, M.G. Panthani, B. Koo, J.W. Tunnell, B.A. Korgel, Copper selenide nanocrystals for photothermal therapy, Nano Lett. 11 (2011) 2560–2566.
[17] G. Liu, J. Zou, Q. Tang, X. Yang, Y. Zhang, Q. Zhang, W. Huang, P. Chen, J. Shao, X. Dong, Surface modified Ti$_3$C$_2$ MXene nanosheets for tumor targeting photothermal/photodynamic/chemo synergistic therapy, ACS Appl. Mater. Interfaces 9 (2017) 40077–40086.
[18] X. Han, X. Huang, J. Huang, H. Lin, Z. Wang, P. Li, Y. Chen, 2D ultrathin MXene-based drug-delivery nanoplatform for synergistic photothermal ablation and chemotherapy of cancer, Adv. Healthc. Mater. 7 (2018) 1701394.
[19] X. Wang, D. Zhang, Q. Xiang, Z. Zhong, Y. Liao, Review of water-assisted crystallization for TiO$_2$ nanotubes, Nano-Micro Lett. 10 (2018) 77.
[20] D. Ding, W. Huang, C. Song, M. Yan, C. Guo, S. Liu, Non-stoichiometric MoO$_{3-x}$ quantum dots as a light-harvesting material for interfacial water evaporation, Chem. Commun. 53 (2017) 6744–6747.
[21] J. Wang, Y. Li, L. Deng, N. Wei, Y. Weng, S. Dong, D. Qi, J. Qiu, X. Chen, T. Wu, High-performance photothermal conversion of narrow-bandgap Ti$_2$O$_3$ nanoparticles, Adv. Mater. 29 (2016) 1603730.
[22] Y. Shi, R. Li, Y. Jin, S. Zhuo, L. Shi, J. Chang, S. Hong, K.-C. Ng, P. Wang, A 3D photothermal structure toward improved energy efficiency in solar steam generation, Joule 2 (2018) 1171–1186.
[23] Y. Shi, R. Li, L. Shi, E. Ahmed, Y. Jin, P. Wang, Composite materials: a robust CuCr$_2$O$_4$/SiO$_2$ composite photothermal material with underwater black property and extremely high thermal stability for solar-driven water evaporation, Adv. Sustain. Syst. 2 (2018) 1870026.
[24] R. Li, L. Zhang, L. Shi, P. Wang, MXene Ti$_3$C$_2$: an effective 2D light-to-heat conversion material, ACS Nano 11 (2017) 3752–3759.
[25] C. Mu, Y. Song, K. Deng, S. Lin, Y. Bi, F. Scarpa, D. Crouse, High solar desalination efficiency achieved with 3D Cu$_2$ZnSnS$_4$ nanosheet-assembled membranes, Adv. Sustain. Syst. (2017) 1700064.
[26] Y. Yang, H. Zhao, Z. Yin, J. Zhao, X. Yin, N. Li, D. Yin, Y. Li, B. Lei, Y. Du, W. Que, A general salt-resistant hydrophilic/hydrophobic nanoporous double layer design for efficient and stable solar water evaporation distillation, Mater. Horiz. 5 (2018) 1143–1150.
[27] J. Zhang, W. Que, Q. Jia, X. Ye, Y. Ding, Controllable hydrothermal synthesis of ZnO nanowires arrays on Al-doped ZnO seed layer and patterning of ZnO nanowires arrays via surface modification of substrate, Appl. Surf. Sci. 257 (2011) 10134–10140.
[28] J. Zhao, Y. Yang, C. Yang, Y. Tian, Y. Han, J. Liu, X. Yin, W. Que, A hydrophobic surface enabled salt-blocking 2D Ti$_3$C$_2$ MXene membrane for efficient and stable solar desalination, J. Mater. Chem. A 6 (2018) 16196–16204.
[29] M. Grossberg, J. Krustok, J. Raudoja, K. Timmo, M. Altosaar, T. Raadik, Photoluminescence and Raman study of Cu$_2$ZnSn(Se$_x$S$_{1-x}$)$_4$ monograins for photovoltaic applications, Thin Solid Films 519 (2011) 7403–7406.
[30] P.A. Fernandes, P.M.P. Salome, A.F. da Cunha, Study of polycrystalline Cu$_2$ZnSnS$_4$ films by Raman scattering, J. Alloys Compd. 509 (2011) 7600–7606.
[31] K. Woo, Y. Kim, J. Moon, A non-toxic, solution-processed, earth abundant absorbing layer for thin-film solar cells, Energy Environ. Sci. 5 (1) (2012) 5340–5345.
[32] J.M.R. Tan, Y.H. Lee, S. Pedireddy, T. Baikie, X.Y. Ling, L.H. Wong, Understanding the synthetic pathway of a single-phase quarternary semiconductor using surface-enhanced Raman scattering: a case of wurtzite Cu$_2$ZnSnS$_4$ nanoparticles, J. Am. Chem. Soc. 136 (2014) 6684–6692.
[33] Y. Qu, G. Zoppi, R.W. Miles, N.S. Beattie, Influence of reaction conditions on the properties of solution-processed Cu$_2$ZnSnS$_4$ nanocrystals, Mater. Res. Express 1 (2014) 045040.
[34] V. Tunuguntla, W.C. Chen, P.H. Shih, I. Shown, Y.R. Lin, J.S. Hwang, C.H. Lee, L.C. Chen, K.H. Chen, A nontoxic solvent based sol–gel Cu$_2$ZnSnS$_4$ thin film for high efficiency and scalable low-cost photovoltaic cells, J. Mater. Chem. A 3 (2015) 15324–15330.
[35] W.C. Chen, V. Tunuguntla, M.-H. Chiu, L.-J. Li, I. Shown, C.-H. Lee, J.-S. Hwang, L.-C. Chen, K.-H. Chen, Co-solvent effect on microwave-assisted Cu$_2$ZnSnS$_4$ nanoparticles synthesis for thin film solar cell, Sol. Energy Mater. Sol. Cells 161 (2017) 416–423.
[36] D. Dumcenco, Y.-S. Huang, The vibrational properties study of kesterite Cu$_2$ZnSnS$_4$ single crystals by using polarization dependent Raman spectroscopy, Opt. Mater. 35 (2013) 419–425.
[37] M. Grossberg, J. Krustok, J. Raudoja, T. Raadik, The role of structural properties on deep defect states in Cu$_2$ZnSnS$_4$ studied by photoluminescence spectroscopy, Appl. Phys. Lett. 101 (2012) 102102–102104.
[38] A. Khare, B. Himmetoglu, M. Johnson, D.J. Norris, M. Cococcioni, E.S. Aydil, Calculation of the lattice dynamics and Raman spectra of copper zinc tin chalcogenides and comparison to experiments, J. Appl. Phys. 111 (2012) 083707–083709.
[39] R. Ahmad, M. Distaso, H. Azimi, C.J. Brabec, W. Peukert, Facile synthesis and post-processing of eco-friendly, highly conductive copper zinc tin sulphide nanoparticles, J. Nanopart. Res. 15 (2013) 1886.
[40] X. Fontané, L. Calvo-Barrio, V. Izquierdo-Roca, E. Saucedo, A. Pérez-Rodriguez,

J.R. Morante, D.M. Berg, P.J. Dale, S. Siebenritt, In-depth resolved Raman scattering analysis for the identification of secondary phases: characterization of Cu_2ZnSnS_4 layers for solar cell applications, Appl. Phys. Lett. 98 (2011) 181905.

[41] D. Moldovan, V. Yamakov, D. Wolf, S.R. Phillpot, Scaling behavior of grain-rotation-induced grain growth, Phys. Rev. Lett. 89 (2002) 206101.

[42] W.C. Liu, B.L. Guo, X.S. Wu, F.M. Zhang, C.L. Mak, K.H. Wong, Facile hydrothermal synthesis of hydrotropic Cu_2ZnSnS_4 nanocrystal quantum dots: band-gap engineering and phonon confinement effect, J. Mater. Chem. A 1 (2013) 3182–3186.

[43] X. Lu, Z. Zhuang, Q. Peng, Y. Li, Wurtzite Cu_2ZnSnS_4 nanocrystals: a novel quaternary semiconductor, Chem. Commun. 47 (2011) 3141–3143.

[44] M. Li, W.H. Zhou, J. Guo, Y.-L. Zhou, Z.-L. Hou, J. Jiao, Z.-J. Zhou, Z.-L. Du, S.-X. Wu, Synthesis of pure metastable wurtzite CZTS nanocrystals by facile one-pot method, J. Phys. Chem. C 116 (2012) 26507–26516.

[45] A. Singh, H. Geaney, F. Laffir, K.M. Ryan, Colloidal synthesis of wurtzite Cu_2ZnSnS_4 nanorods and their perpendicular assembly, J. Am. Chem. Soc. 134 (2012) 2910–2913.